The impact of solvent vapor on the film morphology and crystallization kinetics of lead halide perovskites during annealing

Yu Zhong,[†,§,‡] Dominik Seeberger,[†] Eva M. Herzig,[∥] Anna Köhler,[§,ξ] Fabian Panzer,[*,§] Cheng Li,[*,†,#,$] Sven Huettner[*,†,⊥]

[†] Department of Chemistry, University of Bayreuth, Universitätsstr. 30, Bayreuth 95440, Germany

[§] Soft Matter Optoelectronics, University of Bayreuth, Universitätsstr. 30, Bayreuth 95440, Germany

[‡] Institute of Novel Semiconductors, State Key Laboratory of Crystal Materials, Shandong University, Jinan, 250100, China

[∥] Dynamics and Structure Formation, University of Bayreuth, Universitätsstr.30, Bayreuth 95440, Germany

[ξ] Bavarian Polymer Institute and Bayreuth Institute of Macromolecular Research, University of Bayreuth, Universitätsstr.30, Bayreuth 95440, Germany

[#] School of Electronic Science and Engineering, Xiamen University, Xiamen, 361005, China

[$] Future Display Institute of Xiamen, Xiamen, 361005, P. R. China

[⊥] *current address:* Vishay Semiconductor GmbH, 74072 Heilbronn, Germany

Abstract

One of the key factors for the remarkable improvements of halide perovskites solar cells over the last few years is the increased control over perovskite crystallinity and its thin film morphology. Among various processing methods, solvent vapor assisted annealing (SVAA) has proven to be promising in achieving high quality perovskite films. However, a comprehensive understanding of the perovskite crystallization process during SVAA is still lacking. In this work, we use a home-built setup to precisely control the SVAA conditions to investigate in detail the perovskite crystallization kinetics. By changing the solvent vapor concentration during annealing, the perovskite grain size can be tuned from 200 nm to several micrometers. We monitor the crystallization kinetics during solvent-free annealing and SVAA using *in-situ* grazing incidence wide-angle X-ray scattering, where we find a diminished perovskite growth rate and the formation of low dimensional perovskite at the top of the perovskite layer during SVAA. Scanning electron microscopy of the final films further suggest that the perovskite growth follows an Ostwald ripening process at higher solvent concentrations. Thus, our results will contribute to achieve a more targeted processing of perovskite films.

Introduction

Since their first demonstration in 2012, metal halide perovskites have shown an unprecedented development in solid-state solar cells in terms of both, efficiency and stability.[1,2] It is widely accepted that these properties are closely associated with the crystallinity of the perovskite. Thus, improving perovskite processing to realize highly crystalline thin films is in the current focus of interest. Different approaches such as precursor modulations, solvent treatments, or additive incorporation were used to optimize the solution processing step.[3–6] Another promising approach to improve the perovskite film quality is to optimize the subsequent annealing step, which typically follows after the solution processing step. Besides controlling temperature and ambient conditions,[7–9] the addition of solvent vapor during annealing, often referred to as solvent vapor assisted annealing (SVAA), has been reported to be particularly helpful.[10–12]

Using N,N-dimethylformamide (DMF) vapor during the annealing step, perovskite grain sizes of more than 1.5 µm,[13,14] improved crystallinity, and reduced defects could be achieved.[15,16] This also lead to an enhancement of perovskite solar cell efficiency when methylammonium lead iodide ($MAPbI_3$) films were exposed to DMF or dimethyl sulfoxide (DMSO) vapor, reaching efficiencies up to 19.2%.[17] Furthermore, SVAA is also a well-established method in the field of organic semiconductors to optimize film morphology,[18–23] underlining its high versatility.[24,25] However, even though studies focusing on the SVAA method for perovskite processing exist, more fundamental investigations clarifying in detail the effect of solvent atmosphere on the perovskite structure formation are still lacking.

When it comes to investigating the perovskite crystallization *in-situ*, grazing incidence wide-angle X-ray scattering (GIWAXS) has emerged as a powerful tool.[26–35] For example, GIWAXS measurements performed during the solution processing and subsequent annealing step, revealed that the perovskite crystallization in the course of annealing proceeds in three steps, namely (i) precursor solution stage, (ii) from solution to an intermediate, (iii) from the intermediate to the perovskite crystal.[30,36–38]Also based on GIWAXS investigations, Meng *et al* found that DMF and DMSO can serve as coordinating molecules, forming intermediate adducts during SVAA.[39]

SVAA of perovskite films is often realized by simply putting few droplets of solvent next to an as-spun perovskite film, covering it with a petri dish, followed by heating.[10,16] This approach in principle is well suitable to impact the perovskite crystallization and hence to investigate SVAA in a qualitative way. However, it does not allow to precisely control and tune the solvent concentration quantitatively, limiting gaining a more fundamental understanding of the SVAA process and holding up an industrial prospect.

Here we use a home-built setup to precisely control the solvent vapor concentration during SVAA of spin coated films of the model halide perovskite $MAPbI_3$ and associate it to the final film morphology. Furthermore, we use *in situ* GIWAXS measurements during SVAA to investigate in detail the perovskite crystallization dynamics and compare them to an annealing procedure that only uses elevated temperature without additional solvent vapor. As this method is most widely used for perovskite film fabrication, we refer to this method as standard annealing. Comparing SVAA and standard annealing allows to systematically identify the evolution of perovskite formation, and reveal the presence of a low dimensional perovskite phase in case of SVAA. Based on our results it is possible to draw a complete picture of the perovskite formation process in the course of SVAA, which will help to augment the processing of high-quality perovskite films to its optimum in the future.

Results

We spin coated perovskite thin films following a two-step method as illustrated in Figure 1a. In the first step a PbI_2 layer is spin coated from a PbI_2/DMF solution, followed by spin coating MAI solution (dissolved in isopropanol) on the PbI_2 layer in the second processing step. The subsequent annealing was then performed in a sample chamber, situated in a home-built setup which allows to control and adjust the atmosphere within the sample chamber (see Figure 1b and Figure S1). Such a setup has already been successfully utilized to control the film formation and thus the morphology of semiconducting polymer thin films.[25,40–42] The inlet of the chamber is connected to two controlled gas flows. Flow 1 supplies pure N_2 gas and flow 2 provides N_2 gas saturated with the solvent vapor, as it passes through a solvent bubbler at temperature T_1. For the following experiments we used $T_1 = 75\ ^oC$, corresponding to a flow 2 vapor pressure of 77.78 hPa. All the pipes and the solvent bubbler were placed in a convection oven, which was set to T_1 to ensure an equilibrated temperature within the entire setup, allowing temperatures significantly above room temperature. By mixing the dry nitrogen (flow 1) and the saturated gas (flow 2), it is possible to adjust the solvent vapor concentration in a wide range. Using the Clausius-Clapeyron relation and the ideal gas law allows to estimate the solvent vapor concentration (see SI for more details). The annealing temperature T_2 is controlled by a hot plate, on which the sample chamber is placed.

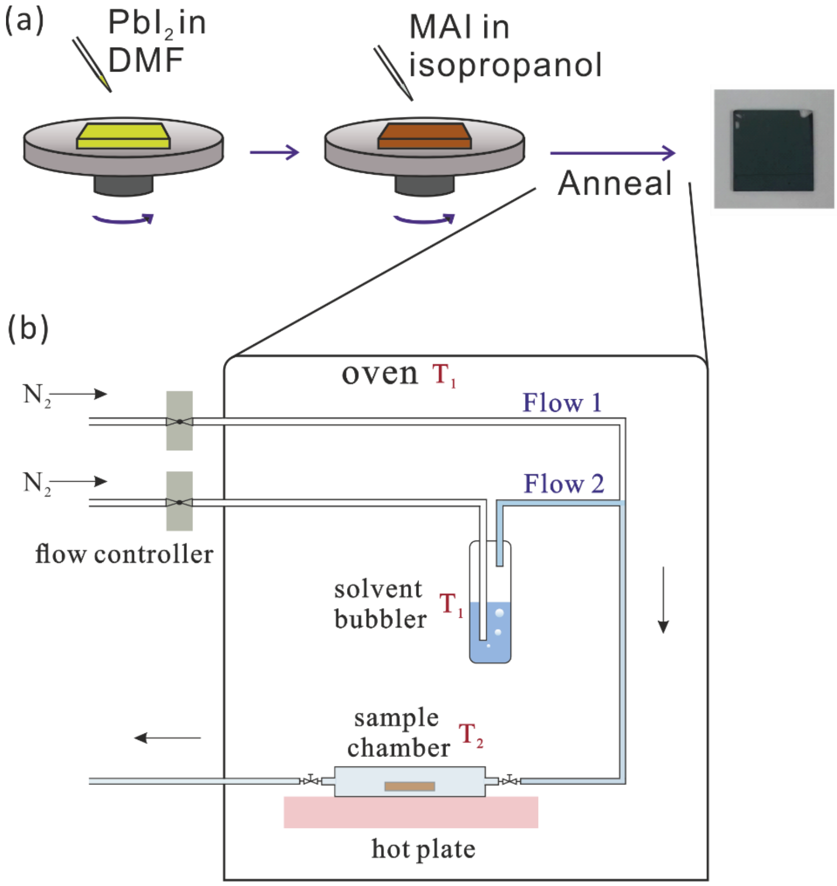

Figure 1: (a) Illustration of the two-step method used to prepare $MAPbI_3$ films in this study; (b) Schematic

illustration of the solvent annealing setup. T_1 is the temperature of the solvent bubbler and of the oven. T_2 is the temperature of the hot plate which controls the temperature of the sample chamber.

In the sample chamber, the films were annealed at $T_2 = 110\ ^{o}C$, where within the first 30 min of annealing DMF vapor was present at a certain constant concentration c_{DMF}, followed by 15 min of annealing with pure N_2 flow. Throughout the entire duration of annealing (45 minutes) the total gas flow (flow 1 + flow 2) was kept at 10 cm^3/min. We chose DMF due to its good solubility of perovskite and PbI_2. To reduce the flow turbulence on the film surface, a low flow rate (flow 1 + flow 2) of 10 cm^3/min was used. Following the approach outlined above we prepared $MAPbI_3$ thin films which were annealed with DMF vapor concentrations c_{DMF} between 0.5×10^{-6} mol/cm^3 and 2.2×10^{-6} mol/cm^3 during the SVAA process (Figure S2).

After the annealing procedure the films were characterized by scanning electron microscopy (SEM), as shown in Figure 2a-g. It becomes clear that in general the grain size increases upon annealing in DMF vapor, however, the surface coverage is reduced for DMF concentrations above 1.1×10^{-6} mol/cm^3. The XRD patterns of the films annealed under high DMF concentrations (1.3×10^{-6}, 1.6×10^{-6}, 2.2×10^{-6} mol/cm^3) indicate a full conversion from PbI_2 and MAI to $MAPbI_3$ (Figure S3).

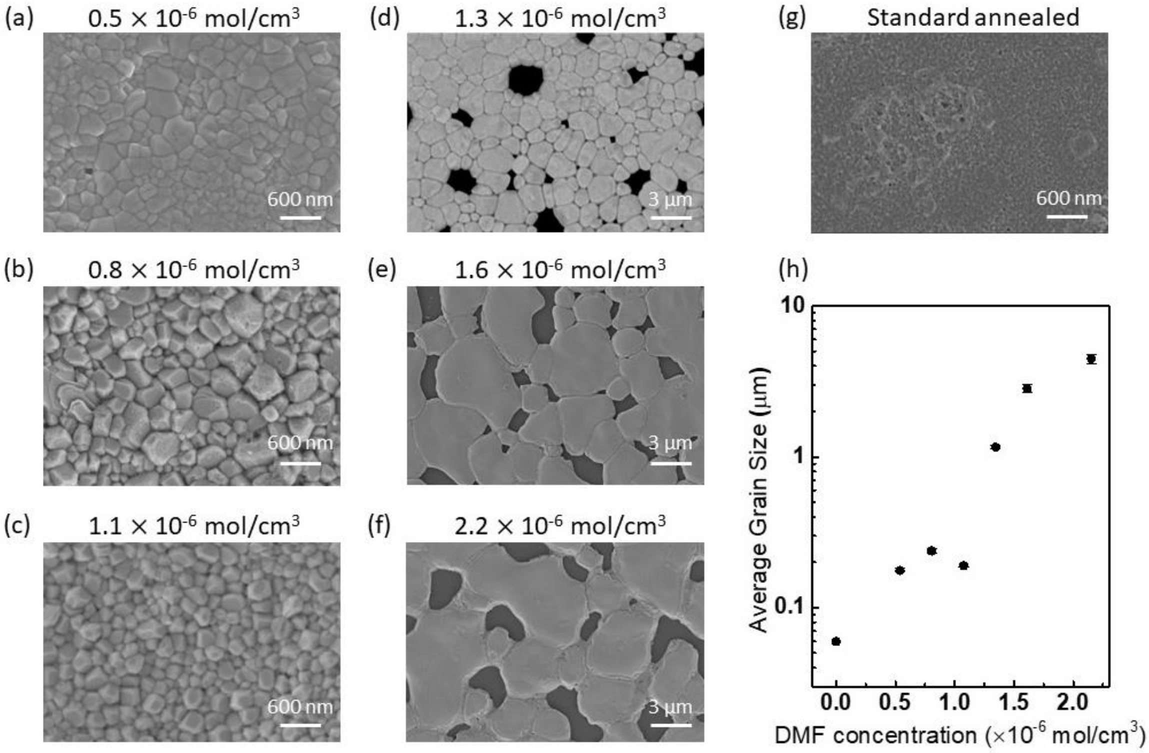

Figure 2: (a)-(f) SEM images of the $MAPbI_3$ films annealed with different DMF concentrations as indicated on top of each image. (g) The SEM image of a standard-annealed perovskite film, i.e., under 0 mol/cm^3 DMF concentration. (h) The average physical grain sizes extracted from the SEM images as a function of different DMF concentrations present during annealing.

Figure 2h shows the average physical grain size extracted from SEM images for the different DMF vapor concentrations used during SVAA. While the film annealed in pure N_2 atmosphere exhibits an average grain size of 60 ± 1 nm, the average grain size increases with DMF concentration, reaching a value of 190±4 nm for the sample annealed with $c_{DMF} = 1.1\times10^{-6}$ mol/cm^3. When the DMF concentration further increases, the average grain size increases further, reaching 4.5 µm at $c_{DMF} = 2.2\times10^{-6}$ mol/cm^3. Furthermore, the shape of the perovskite grains changes to a smoother appearance. If we increase the DMF concentration to 3.8×10^{-6} mol/cm^3, the films become transparent after several minutes of SVAA (Figure S4). Instead of exhibiting granule-like crystals, the resulting morphology appears needle-like on a millimeter scale (Figure S4), which is a sign of dissolution and recrystallization of perovskite-solvent-complex structures.[43] These observations already indicate that while SVAA is an effective method to impact the grain size of the perovskite film, the solvent concentration needs to be carefully controlled.

To investigate the structural evolution of the perovskite film in detail, we use another home-built sample chamber that allows measuring GIWAXS during standard annealing or SVAA *in situ*. To do so, after spin coating MAI solution on the PbI_2 layer, the sample was immediately transferred into the self-designed chamber at the beamline (Figure 3a). The transfer time from the spin coater to the chamber took around 3 min and no obvious change was observed during the transfer.

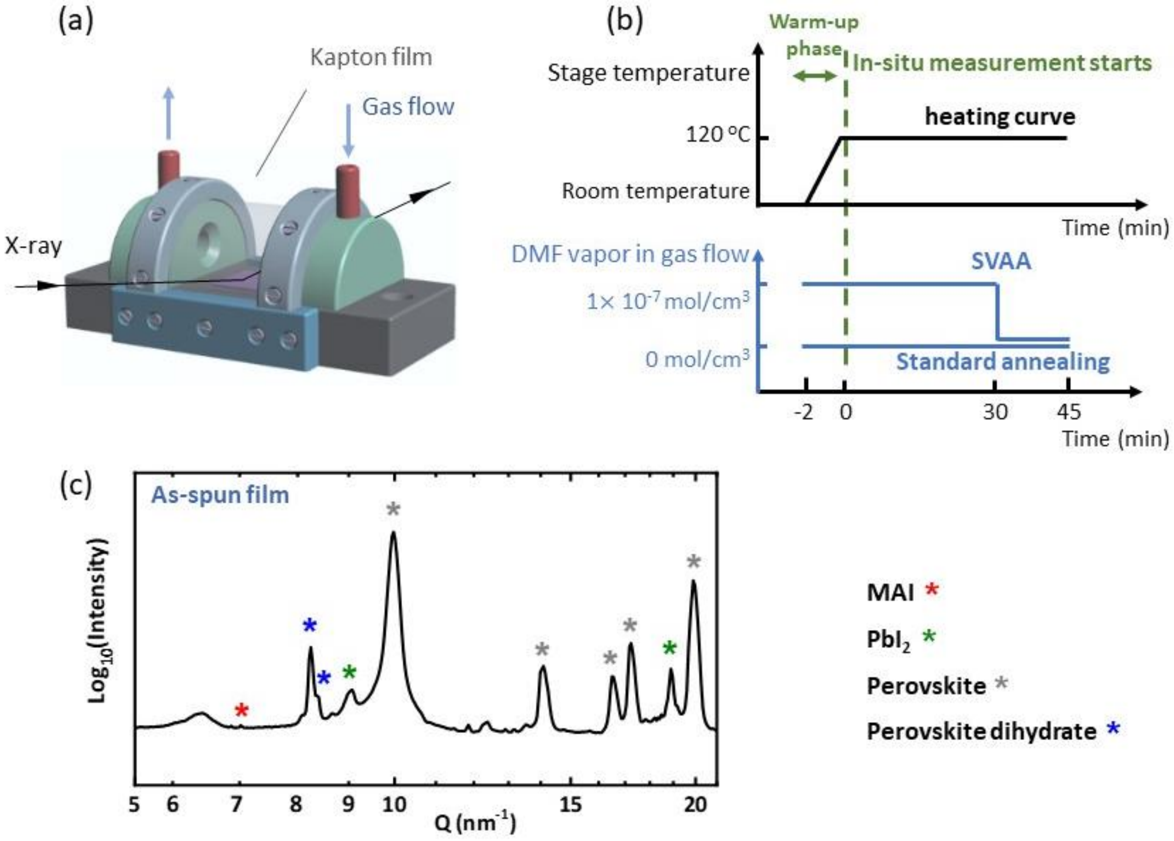

Figure 3: (a) Illustration of the sample chamber used for the *in-situ* GIWAXS measurements. (b) Evolution of the applied stage temperature (black) and DMF vapor concentration (blue) used in this study. The start of the GIWAXS measurements after the warm-up phase to 120°C is also indicated. (c) Azimuthally integrated intensity of the GIWAXS patterns of an as-spun sample, i.e., prior to the annealing process. The asterisks indicate the characteristic peaks of MAI (red), PbI_2 (green), $MAPbI_3$ (grey) and perovskite dihydrate (dark blue).

A semi-cylindric chamber made of Kapton film transmits X-rays while keeping the atmosphere around the sample. The flow inlet of this small chamber is connected to a pure N_2 flow and a N_2 flow saturated with DMF vapor, similar to the setup of Figure 1b (also see Figure S1). The setup restrictions for the X-ray scattering measurement do not allow to control the temperature of the chamber environment as easily as in the oven, hence, the highest achievable DMF concentration was limited to 1×10^{-7} mol/cm^3. The GIWAXS measurements were conducted on two as-spun samples. One was post-processed with annealing at T_2 = 120°C under pure N_2 flow for 45 minutes and the second one was annealed at the same temperature, but applying DMF vapor ($c_{DMF} = 1\times10^{-7}$ mol/cm^3) for 30 minutes followed by 15 minutes of pure N_2 flow (see Figure 3b). Figure 3c shows the azimuthally integrated scattering intensity of a GIWAXS measurement of the film immediately after spin coating. The scattering result is in accordance with the results of our previous study, suggesting that the perovskite crystal starts to form as soon as MAI diffuses into the PbI_2 layer during spin coating.[44] Besides the strong perovskite signal at 9.9 ± 0.1 nm^{-1}, additional peaks at 7.0 ± 0.1 nm^{-1} and 9.0 ± 0.1 nm^{-1} indicate the presence of unreacted MAI and PbI_2 within the film. The peaks at 8.2 ± 0.1 nm^{-1} and 8.4 ± 0.1 nm^{-1} are attributed to the perovskite dihydrate $(MA)_4PbI_6{\cdot}2H_2O$.[45–47] This perovskite dihydrate is likely to form when transferring the as spun-film from the glovebox to the sample chamber. The perovskite dihydrate also contributes to the weak scattering peaks between 12.0 nm^{-1} and 13.8 nm^{-1} and 17.5 nm^{-1} to 18.5 nm^{-1}.

Figure 4a,b show azimuthally integrated intensities of 2D GIWAXS patterns for different annealing times (see Figure S5 for corresponding 2D GIWAXS patterns). The first 2D GIWAXS pattern was recorded immediately when the temperature of the chamber reached 120 ^{o}C (corresponding to t = 0 min). During the warm-up phase, the gas flow (either pure N_2 gas or N_2 gas saturated with DMF) was already applied. At t = 0 min, both samples exhibit the dihydrate peak, but its relative intensity is diminished for the standard annealed sample compared to the SVAA sample. After the post processing, i.e. after 45 min, both standard annealed and SVAA samples show a weak PbI_2 signal, which indicates the degradation of $MAPbI_3$. In a control sample where we measured the annealed perovskite film prepared with the same deposition protocol but without continuous X-ray scattering characterization, no PbI_2 peak was present (Figure S6). This indicates that exposure to X-rays leads to the degradation of $MAPbI_3$ at an elevated temperature, which is in line with literature reports.[48,49] Even though we minimized the X-ray exposure by maximizing the time interval between each measurement and by using short exposure times, we could not avoid the formation of PbI_2 in our *in-situ* measurement. ~~However, as illustrated in Figure 4a,b, the amount of PbI_2 is low compared to the peak intensity of perovskite in both samples after the post processing. Hence, we assume the appearance of PbI_2 has no significant impact on the perovskite crystallization process.~~ As PbI_2 is present already at the start of annealing in abundance, we propose that PbI_2 from degradation has no significant impact on the crystallization behaving similarly to the initial PbI_2. In general, in the two-step method, the perovskite is formed by MAI diffusing into the PbI_2 layer and simultaneously reacting with PbI_2.[50,51] Due to the limited amount of PbI_2 from possible degradation, the effective rate for perovskite formation may only marginally get affected.

To investigate the GIWAXS results in more detail, we consider the temporal evolution of the integrated areas of scattering peaks associated to the perovskite dihydrate at 8.2 ± 0.1 nm^{-1}, PbI$_2$ at 9.0 ± 0.1 nm^{-1}, MAI at 7.0 ± 0.1 nm^{-1} and MAPbI$_3$ at 9.9 ± 0.1 nm^{-1} (Figure 4c,d). After 4 minutes of SVAA, a new scattering peak at 8.1 ± 0.1 nm^{-1} appears, subsequently gaining intensity. Scattering signal at this Q-value was shown in literature to stem from low dimensional perovskite (LDP) phase, forming when MA$^+$ intercalates into PbI$_2$ layers.[52,53] In our measurements, the LDP peak appears and gains intensity after the disappearance of the perovskite dihydrate peak. It needs to be mentioned that the scattering background at 0 min is obviously higher than that after 5 min, indicating possible disordered compounds existing in the film at the beginning.

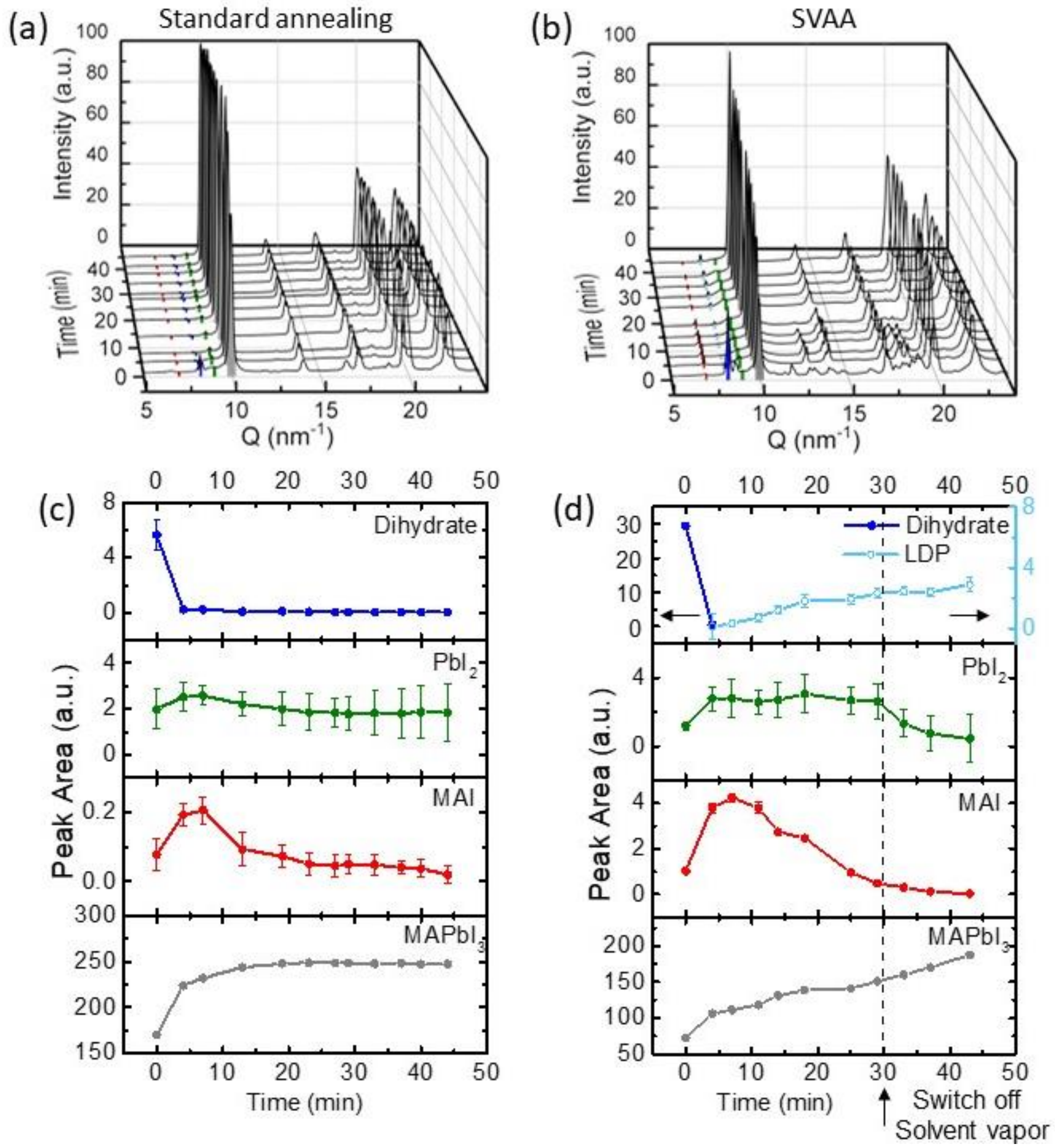

Figure 4: Azimuthally integrated intensity of the GIWAXS patterns of perovskite film during (a) standard annealing and (b) SVAA, together with the temporal evolution of the peak areas corresponding to MAI at 7.0 ± 0.1 nm^{-1} (red), low dimensional perovskite at 8.1 ± 0.1 nm^{-1} (light blue), perovskite dihydrate at 8.2 ± 0.1 nm^{-1} (dark blue), PbI$_2$ at 9.0 ± 0.1 nm^{-1} (green) and MAPbI$_3$ at 9.9±0.1 nm^{-1} (grey).

To elucidate where in the film the LDP forms, we used an as-spun $MAPbI_3$ film and performed SVAA with the same processing settings than before. After 10 minutes of SVAA we measured angle-dependent GIWAXS using a higher intensity of the X-ray source compared to the measurements in Figure 4. This allowed for a faster detection of the scattering patterns, so that within two minutes, three patterns with different incident angles of the X-ray beam (0.15°, followed by 0.3° and 0.6°) could be measured (Figure 5a). With increasing angle, the penetration depth of the 15 keV X-ray beam into the perovskite film increases. An increase from 0.15° to 0.6° corresponds to an increase of the penetration depth from about 27 nm to 352 nm (see Figure S7 for details). Thus, from the decreasing intensity of the scattering peak associated to the LDP for increasing incident X-ray beam angles in Figure 5a, we conclude that the LDP preferably forms at the top of the film. In the standard annealed sample, we could not detect any scattering signal of LDP, even after the signal of the perovskite dihydrate vanished.

Figure 5b shows the evolution of normalized peak area of $MAPbI_3$ for the standard annealing as well as for the SVAA sample, normalized to the value after 4 minutes. It becomes clear that within the first 5 minutes of annealing, the $MAPbI_3$ peak area steeply increases, similarly for both samples. For longer annealing times, the area intensity of the $MAPbI_3$ peak shows a saturation behavior for the standard annealed sample, whereas for the SVAA sample, the area intensity of the $MAPbI_3$ peak increases more continuously without exhibiting a clear saturation behavior. This suggests that upon annealing longer than 4 minutes, the formation kinetics of $MAPbI_3$ are reduced for standard annealing, compared to the SVAA case. We continue our analysis and consider the $MAPbI_3$ peak widths, as they reflect the coherence length of the measured lattice plane, giving information on the crystalline domain size.[54] This is different from the physical grain size obtained from the SEM measurements which can contain several crystalline domains within a single physical grain. As presented in Figure 5c, for both post-processing methods the coherence length increases significantly at the beginning of the annealing process. For standard annealing, the average coherence length of $MAPbI_3$ crystal starts to decrease after 7 minutes, while for SVAA the average coherence length of $MAPbI_3$ crystalline domains reaches higher values and remains more or less unchanged after 7 minutes (also see Figure S8).

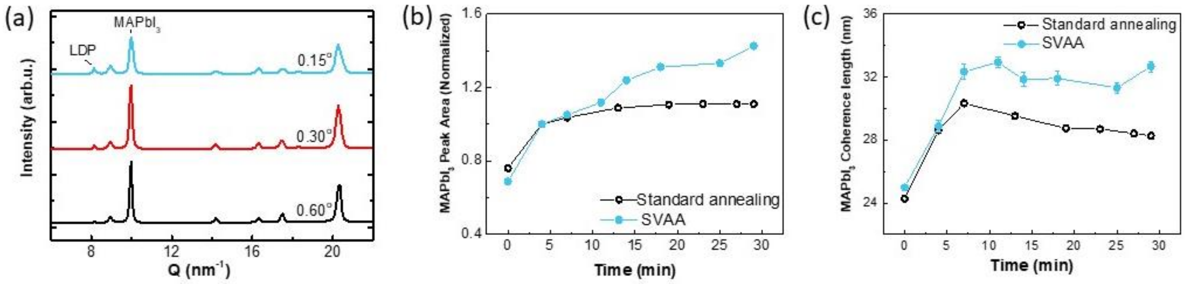

Figure 5: (a) Azimuthally integrated intensity of the GIWAXS patterns with different incident angles of the X-ray beam. The penetration depths corresponding to 0.15°, 0.3° and 0.6° are 82 nm, 223 nm and 471 nm, respectively. (b) The evolution $MAPbI_3$ peak area at 9.9 ± 0.1 nm^{-1} in the first 30 min, normalized to the value after 5 minutes. (c) The evolution of average coherence length of $MAPbI_3$ during standard annealing (black) and SVAA (blue), without correction for constant peak broadening by the set-up.

Examining the MAI peak, both samples show an enhancement of the peak area in the first 7 min followed by a reduction. However, the absolute MAI peak area intensity in SVAA is significantly higher (20-fold after 7 min) than that of standard annealing. The presence of solvent molecules seems to facilitate MAI crystallization.[55] Towards the end of the post-processing, MAI is hardly detected in both samples. Given the error bars of the weak PbI_2 peak at 8.2 ± 0.1 nm^{-1}, the systematic changes of the peak area are not so evident. The low intensity of PbI_2 during annealing is due to the conjoined PbI_2 crystal structure which becomes fractal when MAI diffuses into the PbI_2 layer during spin coating.[44] During annealing, the fractured PbI_2 transforms into perovskite. Compared with the PbI_2 content after annealing, the standard annealed sample shows a more pronounced PbI_2 peak signal than the SVAA sample. The presence of more PbI_2 in the standard-annealed perovskite film is due to its fast formation of $MAPbI_3$. The perovskite film with standard-annealing saturates after 45 minutes of annealing. After its saturation further annealing will lead to potential degradation of $MAPbI_3$, generating PbI_2. For SVAA, the process of $MAPbI_3$ formation is prolonged and thus there is less degradation in this sample.

Discussion

Based on our results, it is possible to draw several conclusions regarding the structure formation occurring during the standard annealing, as well as during the SVAA. According to the phases identified after spin coating (Figure 3c), the as-spun films contain $MAPbI_3$, PbI_2, MAI and perovskite dihydrate (Figure 6a). The $MAPbI_3$ formation during standard annealing and SVAA in principle proceeds in two stages. In stage I, the perovskite dihydrate decomposes and converts into $MAPbI_3$ within the first 4 minutes at 120 °C, as indicated by the decrease of dihydrate scattering signal and concomitant growth of the $MAPbI_3$ scattering signal for both, standard annealing and SVAA. Furthermore, the increase of the MAI scattering signal in the first 4 min can also originate from the decomposition of the perovskite dihydrate, as suggested in the literature, following the reaction,[46]

$$(\mathrm{MA})_4\mathrm{PbI}_6\cdot 2\mathrm{H}_2\mathrm{O} \overset{\Delta}{\leftrightarrow} \mathrm{MAPbI}_3 + 3\mathrm{MAI} + 2\mathrm{H}_2\mathrm{O}.$$

At the beginning of stage II (i.e. after 5 minutes of standard annealing or SVAA) no more perovskite dihydrate is present (Figure 6b). Considering the decrease of scattering background from 0 min to 5min, another possible source of $MAPbI_3$ in stage I is that disordered compound, e.g. perovskite solvate, transfer into ordered perovskite structure upon heating. In contrast, the conversion of MAI and PbI_2 to $MAPbI_3$ takes place throughout both stage I and stage II, independent of the type of annealing. In case of standard annealing, from 5 min to 23 min, the $MAPbI_3$ scattering signal continues to increase and stagnates thereafter, implying that the $MAPbI_3$ formation is completed (Figure 6c).

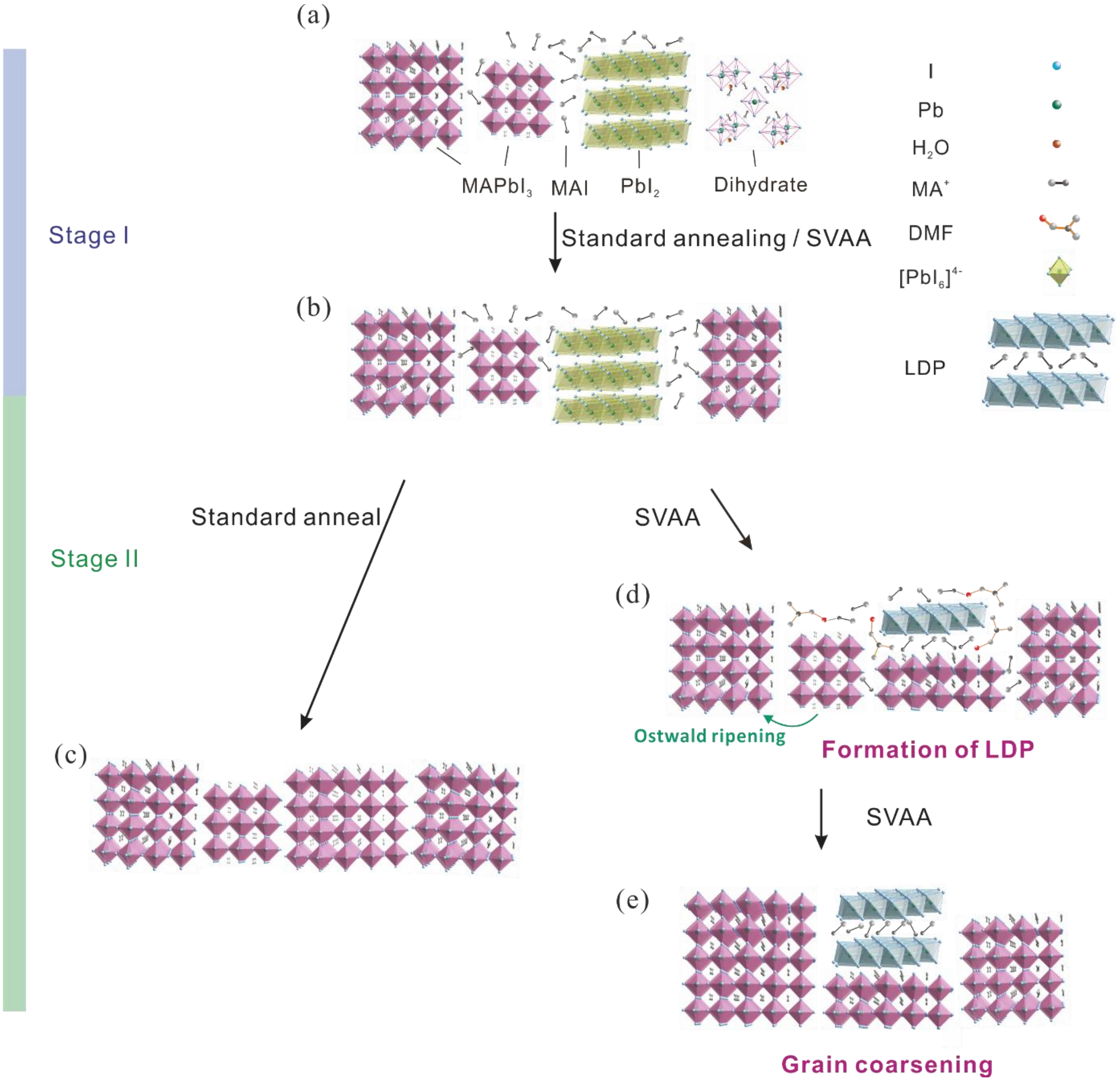

Figure 6: Schematics of $MAPbI_3$ formation during standard annealing and SVAA. The formation process can be divided into two stages. Stage I includes the decomposition of perovskite dihydrate and the reaction between MAI and PbI_2. In stage II, the perovskite formation from MAI and PbI_2 is the main transition. (a) The film before annealing with prevalence of $MAPbI_3$, PbI_2, MAI and perovskite dihydrate. (b) At the end of stage I, when the perovskite dihydrate decomposition is finished. (c) The final state of perovskite film during standard annealing. (d) During SVAA, MA^+ ions intercalate into PbI_2 layer and create a low dimensional perovskite (LDP). The green arrow indicates the Ostwald ripening process. (e) The final state of perovskite film with the SVAA process.

For SVAA at DMF concentrations $\leq 1.1\times10^{-6}$ mol/cm^3, the $MAPbI_3$ thin film formation during stage II, e.g. from 5 min to 30 min, showed a continuous growth, but with a lower crystallization rate compared to the standard annealing case. From 30 min to 45 min, when the DMF vapor is switched off, $MAPbI_3$ continues to form, even with an increased growth rate. This indicates that the $MAPbI_3$ formation in stage II during SVAA does not complete (Figure 6d). This is in line with the results from Guo et al., who found that DMF molecules can be absorbed by MAI, creating a hydrogen bonded DMF-MA^+ complex,[56] also retarding the formation of $MAPbI_3$ from MAI and PbI_2.

Another main difference between the standard annealing and SVAA is the appearance of LDP on top of the film during stage II in case of SVAA (Figure 6d). The formation of LDP has also been detected by Z. Song et al. in standard annealed samples with an excess amount of MAI.[52] LDP was found to emerge when a MA^+ monolayer intercalates into a PbI_2 layered 2D structure.[52,53] Consequently, the spacing between the two $[PbI_6]^{4-}$ octahedral layers is expanded to 0.77 nm, manifested as a scattering peak at 8.1 ± 0.1 nm^{-1}, as observed in our GIWAXS measurements. The formation of LDP during SVAA thus indicates that DMF molecules can assist the intercalation of MA^+ into PbI_2. This appears reasonable, since DMF is able to diffuse into PbI_2, weakening the interaction between the stacked PbI_2 layers.[57] Consequently, the formation of a MA^+ monolayer between PbI_2 sheets is preferred. In a study by Z. Song et al., this LDP is not stable at elevated temperatures and belongs to the δ phase perovskite.[52] Here, the impact of the LDP on the perovskite solar cell properties will be an interesting future aspect to address. Meanwhile, the SVAA results for a low DMF concentration reflect the importance of control of the annealing atmosphere. The annealing of perovskite film in a glovebox with the residual spin-coated solvent inside the glovebox is also a concern for the film formation.

We propose that DMF vapor in SVAA process also mobilizes the grain boundary areas by a dissolution-recrystallization process, resulting in the coarsening of perovskite crystals. (Figure 6d and e). Two aspects support this explanation. On the one hand, the average coherence length of $MAPbI_3$ crystallites during SVAA increases more significantly after 5 minutes with DMF vapor present, compared to the increase for standard annealing (Figure 5c). On the other hand, the SEM images (Figure 2) show that the final morphologies of the $MAPbI_3$ thin films exhibit significantly larger average grain sizes in case of SVAA than for standard annealing. Especially in the case of a high DMF vapor concentration (DMF concentration $> 1.1\times10^{-6}$ mol/cm^3), the pinholes in the final perovskite film imply the formation of a liquid phase when DMF vapor is continuously provided and further liquefied on the film surface. This is well explainable by an Ostwald ripening process.[58] The Ostwald Freundlich equation describes that the equilibrium concentration at the solid-liquid interface of smaller crystals is higher.[59,60] Therefore, smaller crystals keep dissolving to raise the solute concentration for reaching the equilibrium concentration. Thus, during the perovskite film formation, smaller perovskites dissolve in the liquefied DMF and the liquid phase adhere on the larger crystals due to the surface tension. The solute comes to the liquid/crystal interface of the large crystals and further grows, similar to the perovskite single crystal growth from a supersaturated solvent. Moreover, annealing with a higher DMF vapor concentration allows to dissolve more small sized crystals. Thus, with increasing DMF vapor concentration, the average grain size increases and its coverage of the film decreases, as observed in Figure 2.

Conclusion

In this work, we use a dedicated SVAA setup to study the crystallization kinetics of perovskite films. We find that the grain size of perovskite films significantly increases with DMF vapor concentration during the annealing process. Based on *in-situ* GIWAXS measurements, the $MAPbI_3$ crystal growth is decelerated under DMF vapor and DMF molecules assist the formation of low dimensional perovskite phase at the top of the film. For high DMF concentrations, the resulting perovskite film coverage decreases, indicating that DMF dissolves small sized crystals to facilitate growth of large crystals via Ostwald ripening. Our work thus provides insights about the perovskite crystallization kinetics during annealing and how these change when a solvent atmosphere is present, helping to achieve more targeted perovskite film processing in the future.

Corresponding Authors

*C. L., email: chengli@xmu.edu.cn

*F. P., email: fabian.panzer@uni-bayreuth.de

*S. H., email: sven.huettner@uni-bayreuth.de

Acknowledgements

The authors gratefully acknowledge the financial support by Bavarian State Ministry of Science, Research and the Arts for the Collaborative Research Network "Solar Technologies go Hybrid" and German Research Foundation (DFG). Y. Z. acknowledges the funding from China Scholarship Council. C. L. acknowledges funding from National Natural Science Foundation of China (61974126, 51902273). Y. Z., C. L. and S. H. thank German Academic Exchange Service (DAAD) within Bayreuth-Melbourne strategic partnership program for their support. F.P. acknowledges financial support by the DFG via the project PA 3373/3-1. A.K. acknowledges support by the DFG through the project no. 395191217. E. M. H. acknowledges support by the DFG through TUM International Graduate School of Science and Engineering (IGSSE). A part of this research was undertaken on the SAXS/WAXS beamline at the Australian Synchrotron. We thank the Bavarian Polymer Institute for SEM characterizations. We thank Christopher Greve for fruitful discussions.

References

(1) Lee, M. M.; Teuscher, J.; Miyasaka, T.; Murakami, T. N.; Snaith, H. J. Efficient Hybrid Solar Cells Based on Meso-Superstructured Organometal Halide Perovskites. *Science.* **2012**, *338* (6107), 643–647.

(2) Kim, H.-S.; Lee, C.-R.; Im, J.-H.; Lee, K.-B.; Moehl, T.; Marchioro, A.; Moon, S.-J.; Humphry-Baker, R.; Yum, J.-H.; Moser, J. E.; et al. Lead Iodide Perovskite Sensitized All-Solid-State Submicron Thin Film Mesoscopic Solar Cell with Efficiency Exceeding 9%. *Sci. Rep.* **2012**, *2*, 591.

(3) Fassl, P.; Lami, V.; Bausch, A.; Wang, Z.; Klug, M. T.; Snaith, H. J.; Vaynzof, Y. Fractional Deviations in Precursor Stoichiometry Dictate the Properties, Performance and Stability of Perovskite Photovoltaic Devices. *Energy Environ. Sci.* **2018**, *11* (12), 3380–3391.

(4) Pellet, N.; Gao, P.; Gregori, G.; Yang, T.-Y.; Nazeeruddin, M. K.; Maier, J.; Grätzel, M. Mixed-Organic-Cation Perovskite Photovoltaics for Enhanced Solar-Light Harvesting. *Angew. Chemie Int. Ed.* **2014**, *53* (12), 3151–3157.

(5) Jeon, N. J.; Noh, J. H.; Kim, Y. C.; Yang, W. S.; Ryu, S.; Seok, S. Il. Solvent Engineering for High-Performance Inorganic–Organic Hybrid Perovskite Solar Cells. *Nat. Mater.* **2014**, *13* (9), 897–903.

(6) Bai, S.; Da, P.; Li, C.; Wang, Z.; Yuan, Z.; Fu, F.; Kawecki, M.; Liu, X.; Sakai, N.; Wang, J. T.-W.; et al. Planar Perovskite Solar Cells with Long-Term Stability Using Ionic Liquid Additives. *Nature* **2019**, *571* (7764), 245–250.

(7) Huang, L.; Hu, Z.; Xu, J.; Zhang, K.; Zhang, J.; Zhu, Y. Multi-Step Slow Annealing Perovskite Films for High Performance Planar Perovskite Solar Cells. *Sol. Energy Mater. Sol. Cells* **2015**, *141*, 377–382.

(8) You, J.; Yang, Y. (Michael); Hong, Z.; Song, T.-B.; Meng, L.; Liu, Y.; Jiang, C.; Zhou, H.; Chang, W.-H.; Li, G.; et al. Moisture Assisted Perovskite Film Growth for High Performance Solar Cells. *Appl. Phys. Lett.* **2014**, *105* (18), 183902.

(9) Sun, X.; Zhang, C.; Chang, J.; Yang, H.; Xi, H.; Lu, G.; Chen, D.; Lin, Z.; Lu, X.; Zhang, J.; et al. Mixed-Solvent-Vapor Annealing of Perovskite for Photovoltaic Device Efficiency Enhancement. *Nano Energy* **2016**, *28*, 417–425.

(10) Yu, Y.; Wang, C.; Grice, C. R.; Shrestha, N.; Zhao, D.; Liao, W.; Guan, L.; Awni, R. A.; Meng, W.; Cimaroli, A. J.; et al. Synergistic Effects of Lead Thiocyanate Additive and Solvent Annealing on the Performance of Wide-Bandgap Perovskite Solar Cells. *ACS Energy Lett.* **2017**, *2* (5), 1177–1182.

(11) Numata, Y.; Kogo, A.; Udagawa, Y.; Kunugita, H.; Ema, K.; Sanehira, Y.; Miyasaka, T. Controlled Crystal Grain Growth in Mixed Cation-Halide Perovskite by Evaporated Solvent Vapor Recycling Method for High Efficiency Solar Cells. *ACS Appl. Mater. Interfaces* **2017**, *9* (22), 18739–18747.

(12) Luo, J.; Qiu, R. Z.; Yang, Z. S.; Wang, Y. X.; Zhang, Q. F. Mechanism and Effect of γ-Butyrolactone Solvent Vapor Post-Annealing on the Performance of a Mesoporous Perovskite Solar Cell. *RSC Adv.* **2018**, *8* (2), 724–731.

(13) Peng, H.; Lan, C.; Chen, S.; Fan, P.; Liang, G.; Lan, H. N,N-dimethylformamide Vapor Effect on Microstructural and Optical Properties of CH3NH3PbI3 Film during Solvent Annealing. *Surf. Coatings Technol.* **2019**, *359*, 162–168.

(14) Zhang, F.; Song, J.; Zhang, L.; Niu, F.; Hao, Y.; Zeng, P.; Niu, H.; Huang, J.; Lian, J. Film-through Large Perovskite Grains Formation: Via a Combination of Sequential Thermal and Solvent Treatment. *J. Mater. Chem. A* **2016**, *4* (22), 8554–8561.

(15) Tian, L.; Zhang, W.; Yu, H.; Peng, C.; Mao, H.; Li, Y.; Wang, Q.; Huang, Y. Post-Treatment of Perovskite Films toward Efficient Solar Cells via Mixed Solvent Annealing. *ACS Appl. Energy Mater.* **2019**, *2* (7), 4954–4963.

(16) Liu, J.; Gao, C.; He, X.; Ye, Q.; Ouyang, L.; Zhuang, D.; Liao, C.; Mei, J.; Lau, W. Improved Crystallization of Perovskite Films by Optimized Solvent Annealing for High Efficiency Solar Cell. *ACS Appl. Mater. Interfaces* **2015**, *7* (43), 24008–24015.

(17) Zuo, L.; Dong, S.; De Marco, N.; Hsieh, Y. T.; Bae, S. H.; Sun, P.; Yang, Y. Morphology Evolution of High Efficiency Perovskite Solar Cells via Vapor Induced Intermediate Phases. *J. Am. Chem. Soc.* **2016**, *138* (48), 15710–15716.

(18) Li, G.; Shrotriya, V.; Huang, J.; Yao, Y.; Moriarty, T.; Emery, K.; Yang, Y. High-Efficiency Solution Processable Polymer Photovoltaic Cells by Self-Organization of Polymer Blends. *Nat. Mater.* **2005**, *4* (11), 864–868.

(19) Zhao, Y.; Xie, Z.; Qu, Y.; Geng, Y.; Wang, L. Solvent-Vapor Treatment Induced Performance Enhancement of Poly(3-Hexylthiophene):Methanofullerene Bulk-Heterojunction Photovoltaic Cells. *Appl. Phys. Lett.* **2007**, *90* (4), 2005–2008.

(20) Knoll, A.; Horvat, A.; Lyakhova, K. S.; Krausch, G.; Sevink, G. J. A.; Zvelindovsky, A. V; Magerle, R. Phase Behavior in Thin Films of Cylinder-Forming Block Copolymers. *Phys. Rev. l* **2002**, *89* (3), 035501.

(21) Park, J. H.; Kim, J. S.; Lee, J. H.; Lee, W. H.; Cho, K. Effect of Annealing Solvent Solubility on the Performance of Poly(3-Hexylthiophene)/Methanofullerene Solar Cells. *J. Phys. Chem. C* **2009**, *113* (40), 17579–17584.

(22) Crossland, E. J. W.; Rahimi, K.; Reiter, G.; Steiner, U.; Ludwigs, S. Systematic Control of Nucleation Density in Poly(3-Hexylthiophene) Thin Films. *Adv. Funct. Mater.* **2011**, *21* (3), 518–524.

(23) Miller, S.; Fanchini, G.; Lin, Y. Y.; Li, C.; Chen, C. W.; Su, W. F.; Chhowalla, M. Investigation of Nanoscale Morphological Changes in Organic Photovoltaics during Solvent Vapor Annealing. *J. Mater. Chem.* **2008**, *18* (3), 306–312.

(24) Hüttner, S.; Sommer, M.; Chiche, A.; Krausch, G.; Steiner, U.; Thelakkat, M. Controlled Solvent Vapour Annealing for Polymer Electronics. *Soft Matter* **2009**, *5* (21), 4206.

(25) Sepe, A.; Rong, Z.; Sommer, M.; Vaynzof, Y.; Sheng, X.; Müller-Buschbaum, P.; Smilgies, D. M.; Tan, Z. K.; Yang, L.; Friend, R. H.; et al. Structure Formation in P3HT/F8TBT Blends. *Energy Environ. Sci.* **2014**, *7* (5), 1725–1736.

(26) Schlipf, J.; Müller-Buschbaum, P. Structure of Organometal Halide Perovskite Films as Determined with Grazing-Incidence X-Ray Scattering Methods. *Adv. Energy Mater.* **2017**, *7* (16), 1700131.

(27) Barrit, D.; Cheng, P.; Tang, M.; Wang, K.; Dang, H.; Smilgies, D.; Liu, S. (Frank); Anthopoulos, T. D.; Zhao, K.; Amassian, A. Impact of the Solvation State of Lead Iodide on Its Two-Step Conversion to MAPbI 3 : An In Situ Investigation. *Adv. Funct. Mater.* **2019**, *29* (47), 1807544.

(28) Li, J.; Munir, R.; Fan, Y.; Niu, T.; Liu, Y.; Zhong, Y.; Yang, Z.; Tian, Y.; Liu, B.; Sun, J.; et al. Phase Transition Control for High-Performance Blade-Coated Perovskite Solar Cells. *Joule* **2018**, *2* (7), 1313–1330.

(29) Qin, M.; Tse, K.; Lau, T.; Li, Y.; Su, C.; Yang, G.; Chen, J.; Zhu, J.; Jeng, U.; Li, G.; et al. Manipulating the Mixed-Perovskite Crystallization Pathway Unveiled by In Situ GIWAXS. *Adv. Mater.* **2019**, *31* (25), 1901284.

(30) Filonik, O.; Thordardottir, M. E.; Lebert, J.; Pröller, S.; Weiß, S.; Haur, L. J.; Priyadarshi, A.; Fontaine, P.; Müller-Buschbaum, P.; Mathews, N.; et al. Evolution of Perovskite Crystallization in Printed Mesoscopic Perovskite Solar Cells. *Energy Technol.* **2019**, *7* (10), 1900343.

(31) Munir, R.; Sheikh, A. D.; Abdelsamie, M.; Hu, H.; Yu, L.; Zhao, K.; Kim, T.; Tall, O. El; Li, R.; Smilgies, D.-M.; et al. Hybrid Perovskite Thin-Film Photovoltaics: In Situ Diagnostics and Importance of the Precursor Solvate Phases. *Adv. Mater.* **2017**, *29* (2), 1604113.

(32) Pool, V. L.; Dou, B.; Van Campen, D. G.; Klein-Stockert, T. R.; Barnes, F. S.; Shaheen, S. E.; Ahmad, M. I.; van Hest, M. F. A. M.; Toney, M. F. Thermal Engineering of FAPbI3 Perovskite Material via Radiative Thermal Annealing and in Situ XRD. *Nat. Commun.* **2017**, *8* (1), 14075.

(33) Hu, Q.; Zhao, L.; Wu, J.; Gao, K.; Luo, D.; Jiang, Y.; Zhang, Z.; Zhu, C.; Schaible, E.; Hexemer, A.; et al. In Situ Dynamic Observations of Perovskite Crystallisation and Microstructure Evolution Intermediated from [PbI6]4− Cage Nanoparticles. *Nat. Commun.* **2017**, *8* (1), 15688.

(34) Barrows, A. T.; Lilliu, S.; Pearson, A. J.; Babonneau, D.; Dunbar, A. D. F.; Lidzey, D. G. Monitoring the Formation of a CH 3 NH 3 PbI 3- x Cl x Perovskite during Thermal Annealing Using X-Ray Scattering. *Adv. Funct. Mater.* **2016**, *26* (27), 4934–4942.

(35) Tan, W. L.; Kirby, N. M.; Cheng, Y.-B.; McNeill, C. R. Origin of Vertical Slab Orientation in Blade-Coated Layered Hybrid Perovskite Films Revealed with in-Situ Synchrotron X-Ray Scattering. *Nano Energy* **2021**, *83*, 105818.

(36) Chang, C. Y.; Huang, Y. C.; Tsao, C. S.; Su, W. F. Formation Mechanism and Control of Perovskite Films from Solution to Crystalline Phase Studied by in Situ Synchrotron Scattering. *ACS Appl. Mater. Interfaces* **2016**, *8* (40), 26712–26721.

(37) Qin, M.; Xue, H.; Zhang, H.; Hu, H.; Liu, K.; Li, Y.; Qin, Z.; Ma, J.; Zhu, H.; Yan, K.; et al. Precise Control of Perovskite Crystallization Kinetics via Sequential A-Site Doping. *Adv. Mater.* **2020**, *32* (42), 2004630.

(38) Moore, D. T.; Sai, H.; Tan, K. W.; Smilgies, D. M.; Zhang, W.; Snaith, H. J.; Wiesner, U.; Estroff, L. A. Crystallization Kinetics of Organic-Inorganic Trihalide Perovskites and the Role of the Lead Anion in Crystal Growth. *J. Am. Chem. Soc.* **2015**, *137* (6), 2350–2358.

(39) Meng, K.; Wu, L.; Liu, Z.; Wang, X.; Xu, Q.; Hu, Y.; He, S.; Li, X.; Li, T.; Chen, G. In Situ Real-Time Study of the Dynamic Formation and Conversion Processes of Metal Halide Perovskite Films. *Adv. Mater.* **2018**, *30* (11), 1706401.

(40) Anthamatten, M.; Letts, S. A.; Cook, R. C. Controlling Surface Roughness in Vapor-Deposited Poly (Amic Acid) Films by Solvent-Vapor Exposure. *Langmuir* **2004**, *20* (15), 6288–6296.

(41) Zomerman, D.; Kong, J.; McAfee, S. M.; Welch, G. C.; Kelly, T. L. Control and Characterization of Organic Solar Cell Morphology Through Variable-Pressure Solvent Vapor Annealing. *ACS Appl. Energy Mater.* **2018**, *1* (10), 5663–5674.

(42) Pröller, S.; Moseguí González, D.; Zhu, C.; Schaible, E.; Wang, C.; Müller-Buschbaum, P.; Hexemer, A.; Herzig, E. M. Note: Setup for Chemical Atmospheric Control during in Situ Grazing Incidence X-Ray Scattering of Printed Thin Films. *Rev. Sci. Instrum.* **2017**, *88* (6), 066101.

(43) Li, Y.; Zhao, Z.; Lin, F.; Cao, X.; Cui, X.; Wei, J. In Situ Observation of Crystallization of Methylammonium Lead Iodide Perovskite from Microdroplets. *Small* **2017**, *13* (26), 1–7.

(44) Chauhan, M.; Zhong, Y.; Schötz, K.; Tripathi, B.; Köhler, A.; Huettner, S.; Panzer, F. Investigating Two-Step MAPbI 3 Thin Film Formation during Spin Coating by Simultaneous in Situ Absorption and Photoluminescence Spectroscopy. *J. Mater. Chem. A* **2020**, *8* (10), 5086–5094.

(45) Vincent, B. R.; Robertson, K. N.; Cameron, T. S.; Knop, O. Alkylammonium Lead Halides. Part 1. Isolated PbI6 4− Ions in (CH3NH3)4PbI6•2H2O. *Can. J. Chem.* **1987**, *65* (5), 1042–1046.

(46) Halder, A.; Choudhury, D.; Ghosh, S.; Subbiah, A. S.; Sarkar, S. K. Exploring Thermochromic Behavior of Hydrated Hybrid Perovskites in Solar Cells. *J. Phys. Chem. Lett.* **2015**, *6* (16), 3180–3184.

(47) Leguy, A. M. A.; Hu, Y.; Campoy-Quiles, M.; Alonso, M. I.; Weber, O. J.; Azarhoosh, P.; van Schilfgaarde, M.; Weller, M. T.; Bein, T.; Nelson, J.; et al. Reversible Hydration of CH 3 NH 3 PbI 3 in Films, Single Crystals, and Solar Cells. *Chem. Mater.* **2015**, *27* (9), 3397–3407.

(48) Alsari, M.; Bikondoa, O.; Bishop, J.; Abdi-Jalebi, M.; Ozer, L. Y.; Hampton, M.; Thompson, P.; Hörantner, M. T.; Mahesh, S.; Greenland, C.; et al. In Situ Simultaneous Photovoltaic and Structural Evolution of Perovskite Solar Cells during Film Formation. *Energy Environ. Sci.* **2018**, *11* (2), 383–393.

(49) Tan, W. L.; Choo, Y. Y.; Huang, W.; Jiao, X.; Lu, J.; Cheng, Y. B.; McNeill, C. R. Oriented Attachment as the Mechanism for Microstructure Evolution in Chloride-Derived Hybrid Perovskite Thin Films. *ACS Appl. Mater. Interfaces* **2019**, *11* (43), 39930–39939.

(50) Miyadera, T.; Shibata, Y.; Koganezawa, T.; Murakami, T. N.; Sugita, T.; Tanigaki, N.; Chikamatsu, M. Crystallization Dynamics of Organolead Halide Perovskite by Real-Time X-Ray Diffraction. *Nano Lett.* **2015**, *15* (8), 5630–5634.

(51) Fu, Y.; Meng, F.; Rowley, M. B.; Thompson, B. J.; Shearer, M. J.; Ma, D.; Hamers, R. J.; Wright, J. C.; Jin, S. Solution Growth of Single Crystal Methylammonium Lead Halide Perovskite Nanostructures for Optoelectronic and Photovoltaic Applications. *J. Am. Chem. Soc.* **2015**, *137* (17), 5810–5818.

(52) Song, Z.; Watthage, S. C.; Phillips, A. B.; Tompkins, B. L.; Ellingson, R. J.; Heben, M. J. Impact of Processing Temperature and Composition on the Formation of Methylammonium Lead Iodide Perovskites. *Chem. Mater.* **2015**, *27* (13), 4612–4619.

(53) Klein, J. R.; Flender, O.; Scholz, M.; Oum, K.; Lenzer, T. Charge Carrier Dynamics of Methylammonium Lead Iodide: From PbI 2 -Rich to Low-Dimensional Broadly Emitting Perovskites. *Phys. Chem. Chem. Phys.* **2016**, *18* (16), 10800–10808.

(54) Scardi, P. Chapter 13. Microstructural Properties: Lattice Defects and Domain Size Effects. In *Powder Diffraction*; Royal Society of Chemistry: Cambridge, 2008; pp 376–413.

(55) Lee, A. Y.; Erdemir, D.; Myerson, A. S. Crystals and Crystal Growth. In *Handbook of Industrial Crystallization*; Cambridge University Press, 2019; pp 32–75.

(56) Guo, Y.; Shoyama, K.; Sato, W.; Matsuo, Y.; Inoue, K.; Harano, K.; Liu, C.; Tanaka, H.; Nakamura, E. Chemical Pathways Connecting Lead(II) Iodide and Perovskite via Polymeric Plumbate(II) Fiber. *J. Am. Chem. Soc.* **2015**, *137* (50), 15907–15914.

(57) Shen, D.; Yu, X.; Cai, X.; Peng, M.; Ma, Y.; Su, X.; Xiao, L.; Zou, D. Understanding the Solvent-Assisted Crystallization Mechanism Inherent in Efficient Organic-Inorganic Halide Perovskite Solar Cells. *J. Mater. Chem. A* **2014**, *2* (48), 20454–20461.

(58) Cao, X.; Zhi, L.; Li, Y.; Fang, F.; Cui, X.; Ci, L.; Ding, K.; Wei, J. Fabrication of Perovskite Films with Large Columnar Grains via Solvent-Mediated Ostwald Ripening for E Ffi Cient Inverted Perovskite Solar Cells. **2018**.

(59) Ostwald, W. Über Die Vermeintliche Isomerie Des Roten Und Gelben Quecksilbersoxyds Und Die Oberflächenspannung Fester Körper. *Zeitschrift für Phys. Chemie* **1900**, *34*, 495.

(60) Freundlich, H. *Colloid and Capillary Chemistry*; New York, 1926.

Supporting Information to

The impact of solvent vapor on the film morphology and crystallization kinetics of lead halide perovskites during annealing

Yu Zhong,[†,‡,§] Dominik Seeberger,[†] Eva M. Herzig,[‖] Anna Köhler,[§,ξ] Fabian Panzer,[*,§] Cheng Li,[*,#] Sven Huettner[*,†,⊥]

---

* Author to whom correspondence should be addressed: fabian.panzer@uni-bayreuth.de, cheng.li@xmu.edu.cn, sven.huettner@uni-bayreuth.de and

Experimental Procedures

PbI_2 beads, DMF (anhydrous 99.8%) and 2-propanol (anhydrous 99.5%) were from Sigma Aldrich Company. MAI was from Dyesol Company. PbI_2 beads were dissolved in DMF at 75 °C to get 1M solvent. MAI was dissolved in 2-Propanol to get 0.25M solvent. 80 µL PbI_2 solvent was spin coated on the glass substrate, after the substrate was treated with ozone plasma. Then the sample was annealed at 100°C for 5min and 400 µL MAI solvent was spin coated on the PbI_2 layer. After that, the sample was sealed in the sample chamber in the glovebox. The sample chamber was transferred into the oven and connected to the solvent chamber and N_2 gas. Next, the hotplate and gas flow were opened. The sample was annealed at 110 °C for 45 min with a constant overall gas flow of 10 cm^3/min. For SVAA, the sample was annealed using DMF saturated N_2 gas in the first 30 min and then under pure N_2 flow for 15 min. Throughout the entire duration of annealing (45 minutes) the total gas flow (flow 1 + flow 2) was kept at 10 cm^3/min. DMF concentration is adjusted by altering the ratio of flow 1 to flow 2, indicated by the triangles in Figure S2.

For *in-situ* GIWAXS measurements, samples were put in the chamber, which is shown in Figure 3(a). The chamber was placed on a holder, which could be heated. The annealed temperature for GIWAXS measurement is 120 °C. The reason is that the chamber for GIWAXS measurement is quite thick and the actual temperature in the chamber is below 120 °C, around 110 °C. *In-situ* GIWAXS measurements were performed at SAXS/WAXS beamline at Australian synchrotron. The substrates used for the *in-situ* measurements were FTO glasses with compacted TiO_2 layer. The X-ray energy is 11 keV with an incident angle of 0.22°. The scattered X-rays were detected by a 1M Pilatus detector positioned 36 cm behind the sample. Measurements started when the holder reached 120 °C. A customized version of NIKA software based on Igor Pro from WaveMetrics was used to analyze the data.[1] The angle-dependent GIWAX measurements were employed using X-rays with an energy of 15 keV.

SEM images were taken by Zeiss Leo 1530 scanning electron microscope with a field emission gun. The perovskite films were sputtered with a thin platinum layer before observation. The accelerating voltage for electrons is 3 kV. The grain sizes of perovskite crystals were obtained from the SEM images with the help of ImageJ.

SVAA Setup

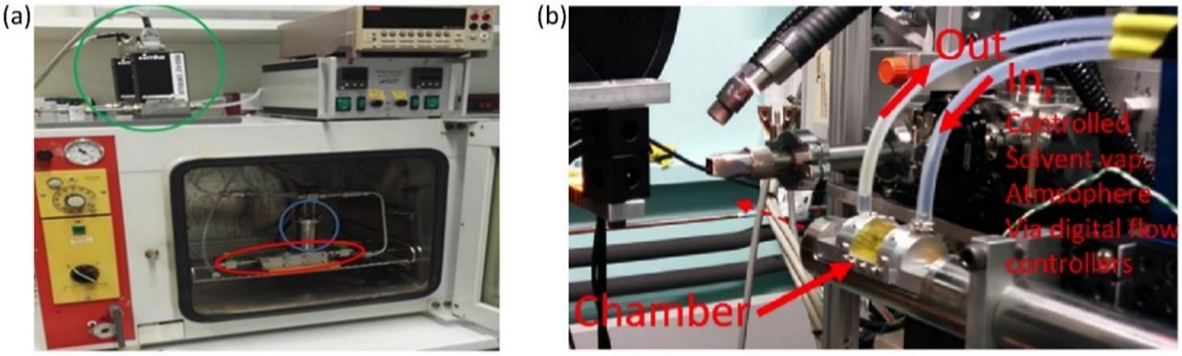

Figure S1: (a) Photographs of the solvent annealing setup shown in Figure 1(b) (main text). In the green circle, there are two flow controllers. In the blue circle is the solvent bubbler. In the red circle is the sample chamber. (b) The SVAA setup for GIWAXS measurements.

Estimation of Solvent Concentration in Chamber

The Clausius-Clapeyron relation shows the vapor pressure change along with temperature[2]

$$ln\frac{p_y}{p_x} = \frac{\Delta H_{vap}}{R}(\frac{1}{T_x} - \frac{1}{T_y})$$

p_y or p_x is the saturated vapor pressure at a given temperature T_x or T_y. T is the temperature. R is the gas constant (8.3145 $J \cdot mol^{-1} \cdot K^{-1}$). ΔH_{vap} is the specific evaporation enthalpy. For DMF, ΔH_{vap}= 46.7 kJ/mol. The vapor pressure at 293.15 K is 3.77 hPa.[3,4]

The setup has exhibited that the saturated gas (flow 2) is diluted by the neat nitrogen (flow 1) before entering the sample chamber. The fraction of the saturated gas used in the sample chamber during the annealing is:

$$sat\% = \frac{F_2}{F_1+F_2} \times 100\% \tag{1}$$

where, F_1 and F_2 are the flow rate of flow 1 and flow 2, respectively.

The actual vapor pressure at temperature T_y with a specific fraction of the saturated gas is:

$$p = sat\% * p_y.$$

Then based on ideal gas concentration: $n = \frac{pV}{RT}$,[2] we can get DMF concentration in the chamber:

$$c = \frac{n}{V} = \frac{p}{RT}.$$

As an example, the DMF vapor concentration in the sample chamber as a function of sat% (the fraction of flow 2) is illustrated in Figure S2. Each line stands for the condition of a different solvent bubbler temperature T$_1$ in our experiment.

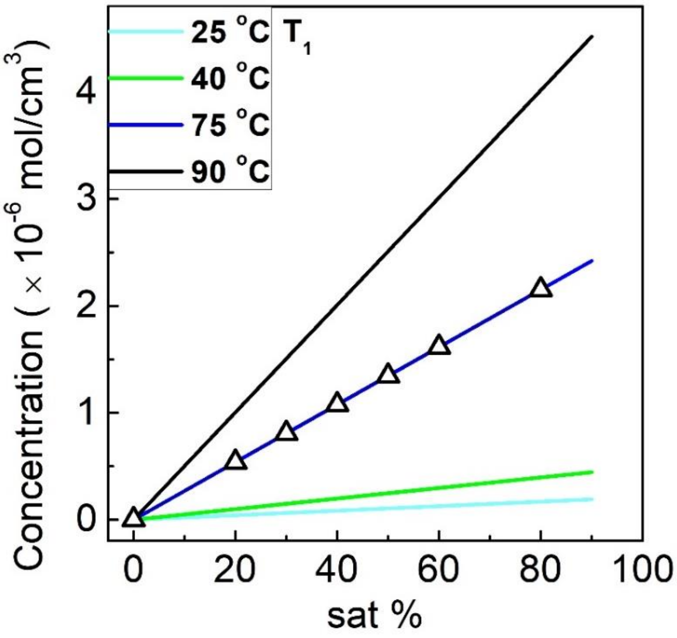

Figure S2: Calculated vapor concentration from Clausius-Clapeyron for different fractions of saturated gas (flow 2) mixed with neat nitrogen (flow 1). Triangles stand for the DMF vapor concentrations used in the experiment.

XRD Patterns of Perovskite Films

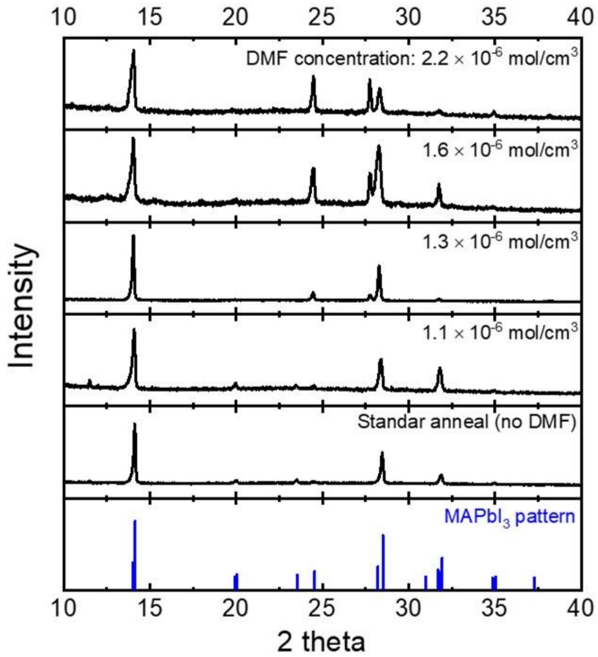

Figure S3: XRD patterns of the perovskite film annealed under different DMF vapor concentration. The data show full conversion into $MAPbI_3$ after annealing. The X-ray energy of the measurements is 8.04 keV.

Morphology of Perovskite Films Annealed under High DMF Vapor

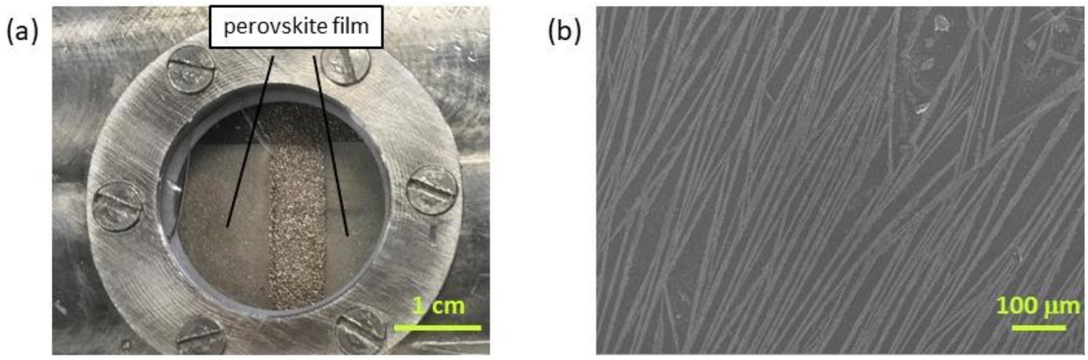

Figure S4: Two Films annealed in parallel with the following condition: DMF concentration = 3.8×10^{-6} mol/cm^3 (Temperature of oven = 90 ^{o}C, DMF saturation = 75%) (a) Photograph taken during the solvent vapor annealing process (b) SEM image of the perovskite film after solvent vapor annealing.

Time-Evolution of GIWAXS Pattern

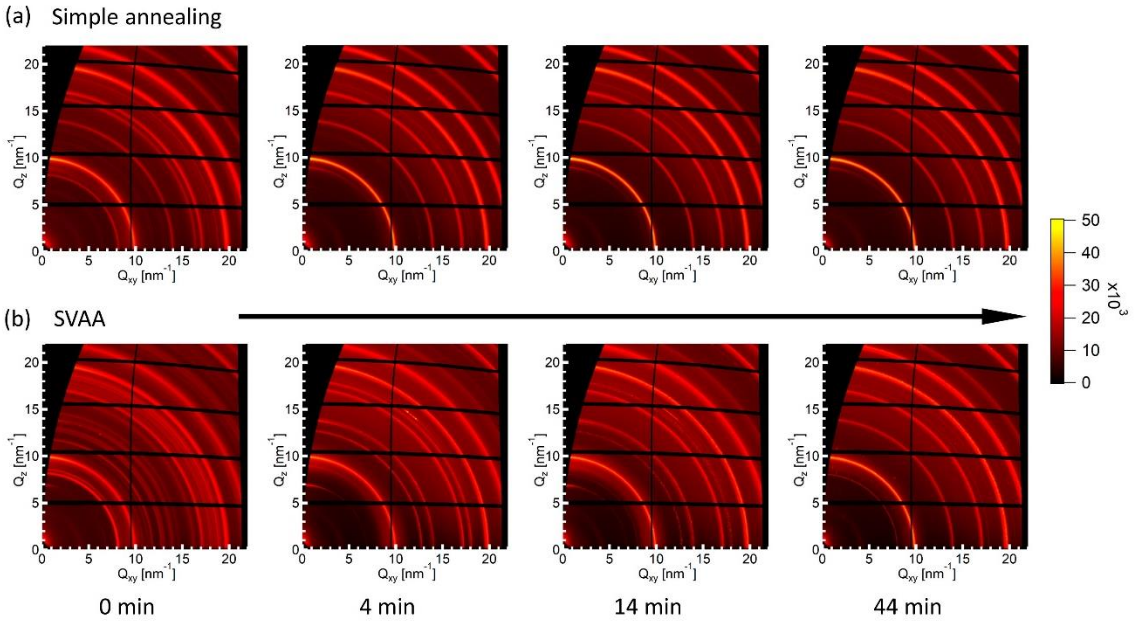

Figure S5: 2D GIWAXS scattering patterns of the sample during (a) standard annealing and (b) SVAA. The arrow indicates that the figures from left to right change along with increasing annealing time.

GIWAXS Patterns of Reference Samples

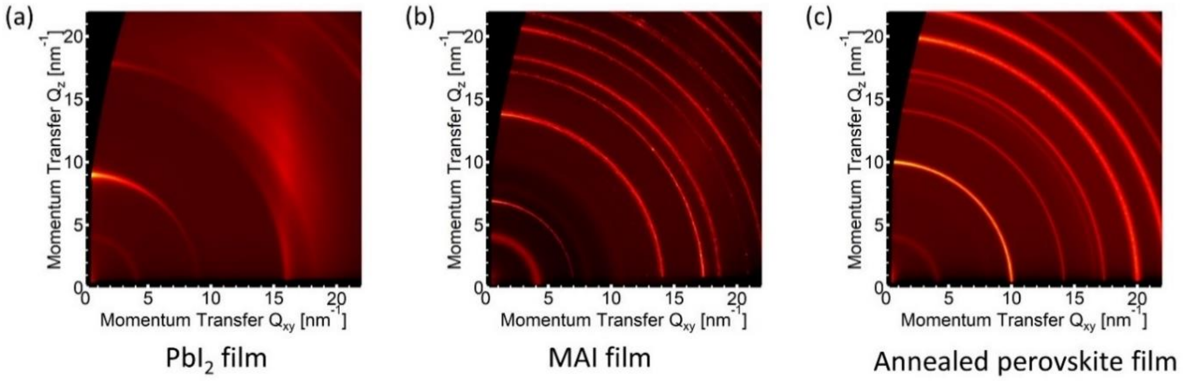

Figure S6: 2D-GIWAXS patterns of (a) PbI_2, (b) MAI, (c) $MAPbI_3$. The annealed perovskite film in (c) was standard annealed before the GIWAXS measurement in a glovebox and no PbI_2 peak was detected in this perovskite film. The peak at 4.0±0.1 nm^{-1} comes from the Kapton window.

Penetration Depth Calculation

The estimation of X-ray penetration depth τ is

$$\tau(\alpha) = \frac{\sqrt{2}\lambda}{4\pi}\left\{\sqrt{(\alpha^2-\alpha_c^2)^2+4\beta^2}-(\alpha^2-\alpha_c^2)\right\}^{-1/2},$$

where λ is the wavelength of X-ray, α is the incident angle, α_c is the critical angle of the perovskite film, β is the imaginary part of refractive index. The critical angle α_c is obtain by $\alpha_c=\sqrt{2\delta}$, where δ is the refractive index decrement. δ and β are derived from the website https://henke.lbl.gov/optical_constants/, with the $MAPbI_3$ density of 4.2 g/cm^3. For X-ray with the energy of 15 keV, δ and β are 3.15×10^{-6} and 1.9×10^{-7}, respectively. Based on these data, the calculated X-ray penetration depth is displayed in Figure S7.

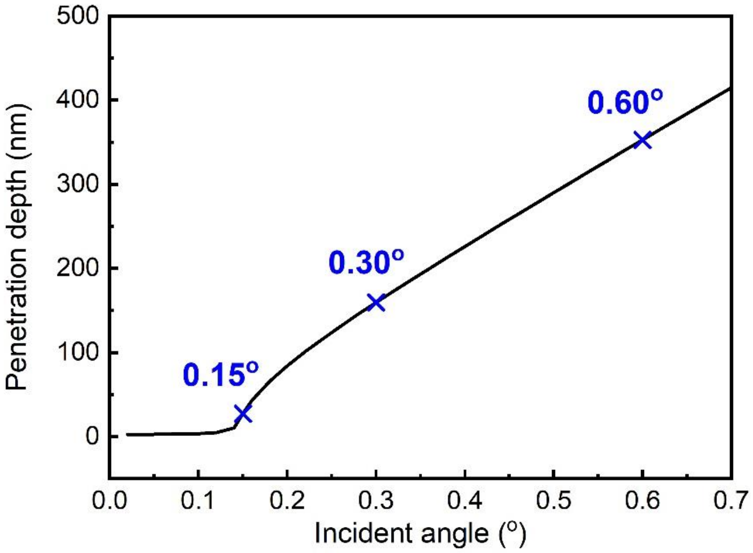

Figure S7: Graph of X-ray penetration depth in GIWAXS measurements as a function of the angle of incidence. The blue intersects represent the penetration depth with the incident angles of 0.15°, 0.30° and 0.60°.

Coherence Length

The coherence length describes the maximum distance between two points which interfere within a grating. One way to extract the coherence length L_C is through Scherrer equation:[5,6]

$$L_C = \frac{2\pi K}{\Delta q}$$

Where K is the shape factor and Δq is the full width at half-maximum of a diffraction peak. In contrast to the average physical grain size obtained from the SEM images, the coherence length extracted from the scattering data is considered as the coherently scattering domain size.

$K = 0.93$ is appropriate for spherical crystals with cubic symmetry and this value is used in the calculation. The coherence length of $MAPbI_3$ crystallites is derived from the scattering peak at 9.9 ± 0.1 nm^{-1} shown in Figure S8 (a) and (b).

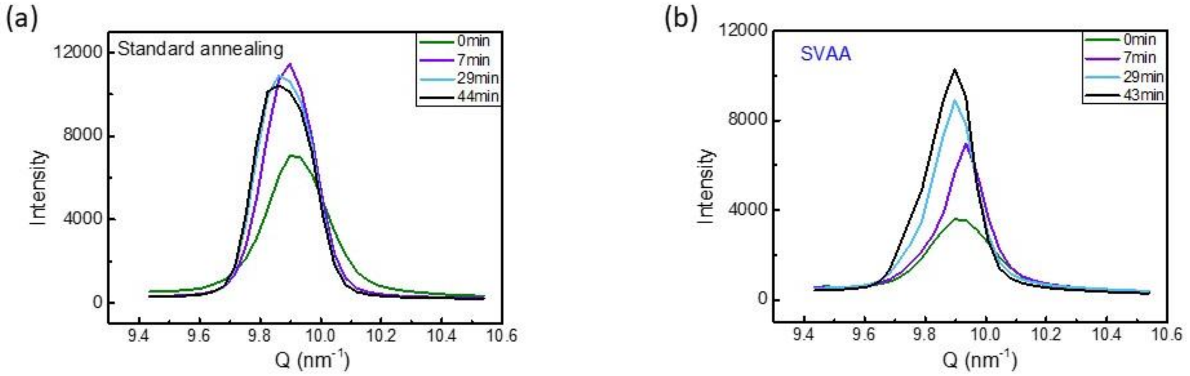

Figure S8: Azimuthally integrated intensity of the $MAPbI_3$ peak at 9.9±0.1 nm^{-1}(a) standard annealing and (b) SVAA.

Azimuthally integrated intensity of GIWAXS in-situ measurements

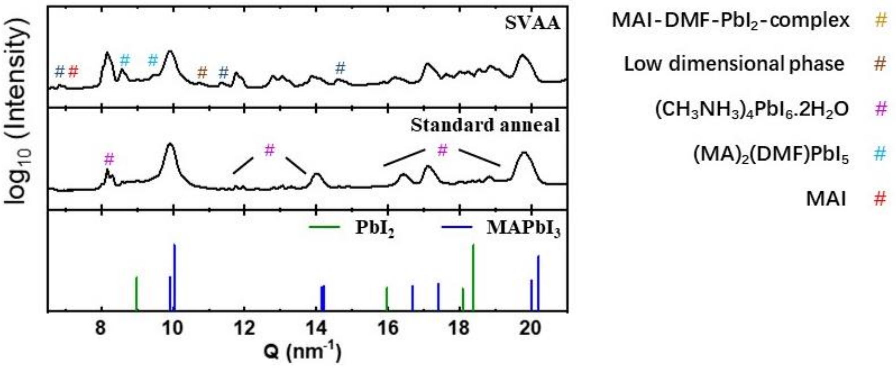

Figure S9: (a) Azimuthally integrated intensity of GIWAXS from *in-situ* measurements shown in Figure S5 (at the 0 min). The hash signs indicate the characteristic peaks of MAI-DMF-PbI_2 complex (yellow), low dimensional phase (orange), $(CH_3NH_3)_4PbI_6.2H_2O$ (purple), $(MA)_2(DMF)PbI_5$ (blue), MAI (red). The bottom part is the theoretical scattering patterns of PbI_2 and $MAPbI_3$.

Supporting References

(1) Gann, E.; Caironi, M.; Noh, Y.-Y.; Kim, Y.-H.; McNeill, C. R. Diffractive X-Ray Waveguiding Reveals Orthogonal Crystalline Stratification in Conjugated Polymer Thin Films. *Macromolecules* **2018**, 51 (8), 2979–2987.

(2) Hentschke, R. *Thermodynamics*; Undergraduate Lecture Notes in Physics; Springer Berlin Heidelberg: Berlin, Heidelberg, **2014**.

(3) Panneerselvam, K.; Antony, M. P.; Srinivasan, T. G.; Vasudeva Rao, P. R. Enthalpies of Vaporization of N,N-Dialkyl Monamides at 298.15K. *Thermochim. Acta* **2009**, 495 (1–2), 1–4.

(4) Daubert, T. E. *Physical and Thermodynamic Properties of Pure Chemicals : Data Compilation*; New York : Hemisphere Pub. Corp., **1989**.

(5) Scherrer, P. Bestimmung Der Größe Und Der Inneren Struktur von Kolloidteilchen Mittels Röntgenstrahlen. *Nachrichten von der Gesellschaft der Wissenschaften zu Göttingen*, Math. Klasse **1918**, 2, 98–100.

(6) Smilgies, D. M. Scherrer Grain-Size Analysis Adapted to Grazing-Incidence Scattering with Area Detectors. *J. Appl. Crystallogr.* **2009**, 42 (6), 1030–1034.